



JWST Imaging of the Cartwheel Galaxy Reveals Dust Associated with SN 2021afdx

Griffin Hosseinzadeh¹ , David J. Sand¹ , Jacob E. Jencson² , Jennifer E. Andrews³ , Irene Shvaei¹ ,
K. Azalee Bostroem^{1,10} , Stefano Valenti⁴ , Tamás Szalai^{5,6,7} , Jamison Burke^{8,9} , D. Andrew Howell^{8,9} ,
Curtis McCully^{8,9} , Megan Newsome^{8,9} , Estefania Padilla Gonzalez^{8,9} , Craig Pellegrino^{8,9} , and Giacomo Terreran^{8,9}

¹ Steward Observatory, University of Arizona, 933 North Cherry Avenue, Tucson, AZ 85721-0065, USA; griffin0@arizona.edu

² Department of Physics and Astronomy, The Johns Hopkins University, 3400 North Charles Street, Baltimore, MD 21218, USA

³ Gemini Observatory, 670 North A'ohoku Place, Hilo, HI 96720-2700, USA

⁴ Department of Physics and Astronomy, University of California, Davis, 1 Shields Avenue, Davis, CA 95616-5270, USA

⁵ Department of Experimental Physics, Institute of Physics, University of Szeged, Dóm tér 9, Szeged, 6720, Hungary

⁶ ELKH-SZTE Stellar Astrophysics Research Group, H-6500 Baja, Szegedi út, Kt. 766, Hungary

⁷ Konkoly Observatory, Research Centre for Astronomy and Earth Sciences, Eötvös Loránd Research Network (ELKH), Konkoly-Thege Miklós út 15-17, 1121 Budapest, Hungary

⁸ Las Cumbres Observatory, 6740 Cortona Drive, Suite 102, Goleta, CA 93117-5575, USA

⁹ Department of Physics, University of California, Santa Barbara, CA 93106-9530, USA

Received 2022 October 12; revised 2022 November 18; accepted 2022 November 20; published 2023 January 3

Abstract

We present near- and mid-infrared (0.9–18 μm) photometry of supernova (SN) 2021afdx, which was imaged serendipitously with the James Webb Space Telescope (JWST) as part of its Early Release Observations of the Cartwheel Galaxy. Our ground-based optical observations show it is likely to be a Type IIb SN, the explosion of a yellow supergiant, and its infrared spectral energy distribution (SED) ≈ 200 days after explosion shows two distinct components, which we attribute to hot ejecta and warm dust. By fitting models of dust emission to the SED, we derive a dust mass of $(3.8^{+0.5}_{-0.3}) \times 10^{-3} M_{\odot}$, which is the highest yet observed in a Type IIb SN but consistent with other Type II SNe observed by the Spitzer Space Telescope. We also find that the radius of the dust is significantly larger than the radius of the ejecta, as derived from spectroscopic velocities during the photospheric phase, which implies that we are seeing an infrared echo off of preexisting dust in the progenitor environment, rather than dust newly formed by the SN. Our results show the power of JWST to address questions of dust formation in SNe, and therefore the presence of dust in the early universe, with much larger samples than have been previously possible.

Unified Astronomy Thesaurus concepts: Core-collapse supernovae (304); Supernovae (1668); Type II supernovae (1731); Dust formation (2269)

Supporting material: data behind figures

1. Introduction

Radio observations of luminous quasars in the early universe (redshift $z \gtrsim 6$, age $\lesssim 1$ Gyr) show them to be large dust reservoirs ($\gtrsim 10^8 M_{\odot}$; Bertoldi et al. 2003; Gall et al. 2011a; Hashimoto et al. 2019; though see Bakx et al. 2020 for a recent counterexample). With progenitor lifetimes of only tens of Myr, dust condensation in the expanding ejecta of core-collapse supernovae (SNe) has been proposed as the major source of dust in these early galaxies (see Gall et al. 2011b for a review). This would require the production of up to $1 M_{\odot}$ of dust per SN, with ejecta models predicting it would condense during the first 1–2 yr after explosion (e.g., Dwek et al. 2007, 2019, but see Wesson & Bevan 2021 and Niculescu-Duvaz et al. 2022 for alternate discussions). However, nebular observations of SNe in the local universe have for the most part not directly confirmed these large dust masses. Compilations of near- and mid-infrared (IR) observations of SNe yield warm dust masses in the range of 10^{-6} – $10^{-2} M_{\odot}$ (Szalai & Vinkó 2013; Tinyanont et al. 2016; Szalai et al. 2019).

When the search for SN dust extends to even older SNe, or into the far-IR or radio wavelengths, there is less of a discrepancy between the required and observed dust masses. For example, unambiguous evidence of 0.4–0.7 M_{\odot} of newly formed cold dust has been confirmed in SN 1987A through observations with Herschel and the Atacama Large Millimeters/submillimeter Array (Matsuura et al. 2011; Indebetouw et al. 2014). Additionally, large masses of cold dust have been detected in much older Galactic SN remnants (Barlow et al. 2010; Gomez et al. 2012; Arendt et al. 2014; Lau et al. 2015; De Looze et al. 2017; Temim et al. 2017), suggesting significant amounts of dust formation occurring in the decades after explosion.

Thermal dust emission typically peaks in the mid-IR (5–10 μm), putting it out of reach of ground-based observations. Until now, the state of the art in observations of dust in extragalactic SNe was using the Spitzer Space Telescope before it ran out of cryogen in 2009 (the Spitzer Cold Mission) to observe the full near-IR to mid-IR spectral energy distribution (SED) of 12 SNe II (Kotak et al. 2005, 2006, 2009; Meikle et al. 2007; Andrews et al. 2011; Meikle et al. 2011; Szalai et al. 2011; see Szalai & Vinkó 2013 and Priestley et al. 2020 for the full sample). Since then, Spitzer has observed dozens more SNe out to 4.5 μm during its Warm Mission (Fox et al. 2010, 2011; Tinyanont et al. 2016; Szalai et al. 2019), but in this wavelength regime, the thermal and line emission from the

¹⁰ LSSTC Catalyst Fellow.



SN ejecta can dominate over any dust emission, so it is difficult to measure dust properties and masses.

An additional complication is the fact that dust masses cannot be fully constrained when the dust is optically thick (e.g., Meikle et al. 2007). A large amount of dust can be hidden behind an optically thick surface layer without changing the observed SED. This happens at dust masses around $10^{-3} M_{\odot}$ (Meikle et al. 2007), although this number also depends on the dust radius and composition. Therefore it is possible that many of the previous dust measurements are in fact lower limits. However, in cases where contemporaneous observations at shorter wavelengths exist, it can be difficult or impossible to reconcile large amounts of optically thick dust with an unextinguished optical SED (e.g., Priestley et al. 2020; Wesson & Bevan 2021).

The first images from the James Webb Space Telescope (JWST) were released on 2022 July 12 (Pontoppidan et al. 2022), reopening our window into the space-based mid-IR. Images of the Cartwheel Galaxy, taken with the Near-Infrared Camera (NIRCam; Rieke et al. 2005) and the Mid-Infrared Instrument (MIRI; Rieke et al. 2015), were released shortly thereafter, on 2022 August 2 (Figure 1). As first noted by Engesser et al. (2022), SN 2021afdx is detected in these images, taken at phases of 197 (NIRCam) and 200 (MIRI) rest-frame days after the last prediscovery nondetection.

In this Letter, we use these images to construct the full near-to mid-IR SED of SN 2021afdx with the goal of constraining dust formation in its ejecta, the first opportunity to do this type of analysis in the past decade. In Section 2.1, we describe our supporting ground-based optical observations, and in Section 2.2, we measure photometry on the space-based IR images. We fit dust models to the resulting SED and compare to previous measurements in Section 3. In Section 4, we investigate whether the dust was newly formed in the SN ejecta or whether it existed in the progenitor environment before explosion. We conclude by looking forward to the future of SN dust measurements with JWST in Section 5.

2. Observations and Data Reduction

2.1. Ground-based Optical

SN 2021afdx was discovered by the Asteroid Terrestrial-impact Last Alert System (ATLAS; Tonry et al. 2018) on 2021 November 23.308 UT at R.A. $00^{\text{h}}37^{\text{m}}42^{\text{s}}.580$ and decl. $-33^{\circ}43'25''28$ (Tonry et al. 2021), $32''$ southeast of the center of the Cartwheel Galaxy (ESO 350-40). We downloaded the full survey light curve from the ATLAS Forced Photometry Server. The explosion time is not very well constrained, as the transient only peaked ≈ 1.5 mag above the typical limiting magnitude of the survey, so we adopt the last prediscovery nondetection on 2021 November 21.352 UT as phase = 0 throughout our analysis.

We also obtained multiband follow-up photometry using the Sinistro cameras on Las Cumbres Observatory’s network of 1 m telescopes (Brown et al. 2013) as part of the Global Supernova Project. We subtracted reference images of the field taken with the same telescopes on 2022 May 27, about 4 months after the SN had faded, using PyZOGY (Guevel & Hosseinzadeh 2017) and measured point spread function (PSF) photometry on the difference images using `lcogtsnpipe` (Valenti et al. 2016). We calibrated this photometry to the AAVSO Photometry All-Sky Survey (Henden et al. 2009).

B and V are reported in Vega magnitudes, and g , r , and i are reported in AB magnitudes.

We adopt a luminosity distance of $d_L = 136.8$ Mpc (distance modulus $\mu = 35.68$ mag) based on the redshift of the Cartwheel Galaxy ($z = 0.030187$; Amram et al. 1998) and the cosmology of the Planck Collaboration et al. (2020). Absolute magnitudes are corrected for Milky Way extinction of $E(B - V) = 0.0092$ mag (Schlafly & Finkbeiner 2011) using the Fitzpatrick (1999) extinction law. Figure 2 (top) shows the ground-based optical light curve.

We construct a pseudobolometric light curve by fitting a blackbody SED to each epoch of photometry to get the photospheric temperature and radius, using a Markov Chain Monte Carlo (MCMC) routine implemented in the Light Curve Fitting package (Hosseinzadeh & Gomez 2022). We then integrate this SED from the U to I bands to obtain a pseudobolometric luminosity that is comparable to previous optical-only data sets. The results are shown in Figure 2 (center and bottom). The peak occurs at a phase of 11.8 days, with a pseudobolometric luminosity of $L_{\text{peak}} = 1.66 \times 10^{42}$ erg s $^{-1}$ and a photospheric temperature of $T_{\text{peak}} = 6900$ K.

SN 2021afdx was classified as an SN II by the Advanced Extended Public ESO Spectroscopic Survey of Transient Objects (ePESTO+; Smartt et al. 2015) based on a spectrum taken with the ESO Faint Object Spectrograph and Camera 2 (EFOSC2; Buzzoni et al. 1984) on the New Technology Telescope on 2021 November 26.173 (Ragosta et al. 2021a). We obtained six additional optical spectra using FLOYDS on Las Cumbres Observatory’s 2 m Faulkes Telescope South (Brown et al. 2013), which are logged in Table 1 and plotted in Figure 3. The spectra are available in machine-readable form in the online journal and on the Weizmann Interactive Supernova Data Repository (Yaron & Gal-Yam 2012).

Type IIb SNe are a transitional class of core-collapse explosions in which early spectra show strong hydrogen lines that fade away in later spectra (see Gal-Yam 2016 for a review). These are thought to come from partially stripped yellow supergiant progenitors (see reviews by Smartt 2009 and Van Dyk 2016). Ragosta et al. (2021b) raised the possibility of a Type IIb subclassification for SN 2021afdx in their initial AstroNote, based on spectroscopic similarities to SN 2008aq. Several aspects of our data support this classification. First, the absorption component of the $H\alpha$ P Cygni profile is very strong, broad, and asymmetrical compared to typical SN II, and more closely resembles Type IIb spectra. We show this in Figure 3, where we compare to early spectra of the Type IIb SN 2016gkg (Tartaglia et al. 2017) and the Type II SN 2021yja (Hosseinzadeh et al. 2022). The helium-to-hydrogen line ratio is also high and increasing in our spectral series, suggesting that the hydrogen features might have faded after the end of our observing campaign. Our earliest spectrum of SN 2021afdx is redder (Figure 3) and the photospheric temperature is lower (Figure 2, bottom) than typical SNe II at this phase. Lastly, the gradual rise and decline of the bolometric light curve of SN 2021afdx more closely resembles the Type IIb SN 1993J¹¹ than the Type II SN 2021yja (Hosseinzadeh et al. 2022), which rose quickly to a plateau (see Figure 2, center). However, as we never see the hydrogen features fully disappear, even by day

¹¹ We constructed the pseudobolometric light curve of SN 1993J using data from Okyudo et al. (1993), van Driel et al. (1993), Benson et al. (1994), Lewis et al. (1994), Richmond et al. (1994, 1996), Barbon et al. (1995), and Metlova et al. (1995).

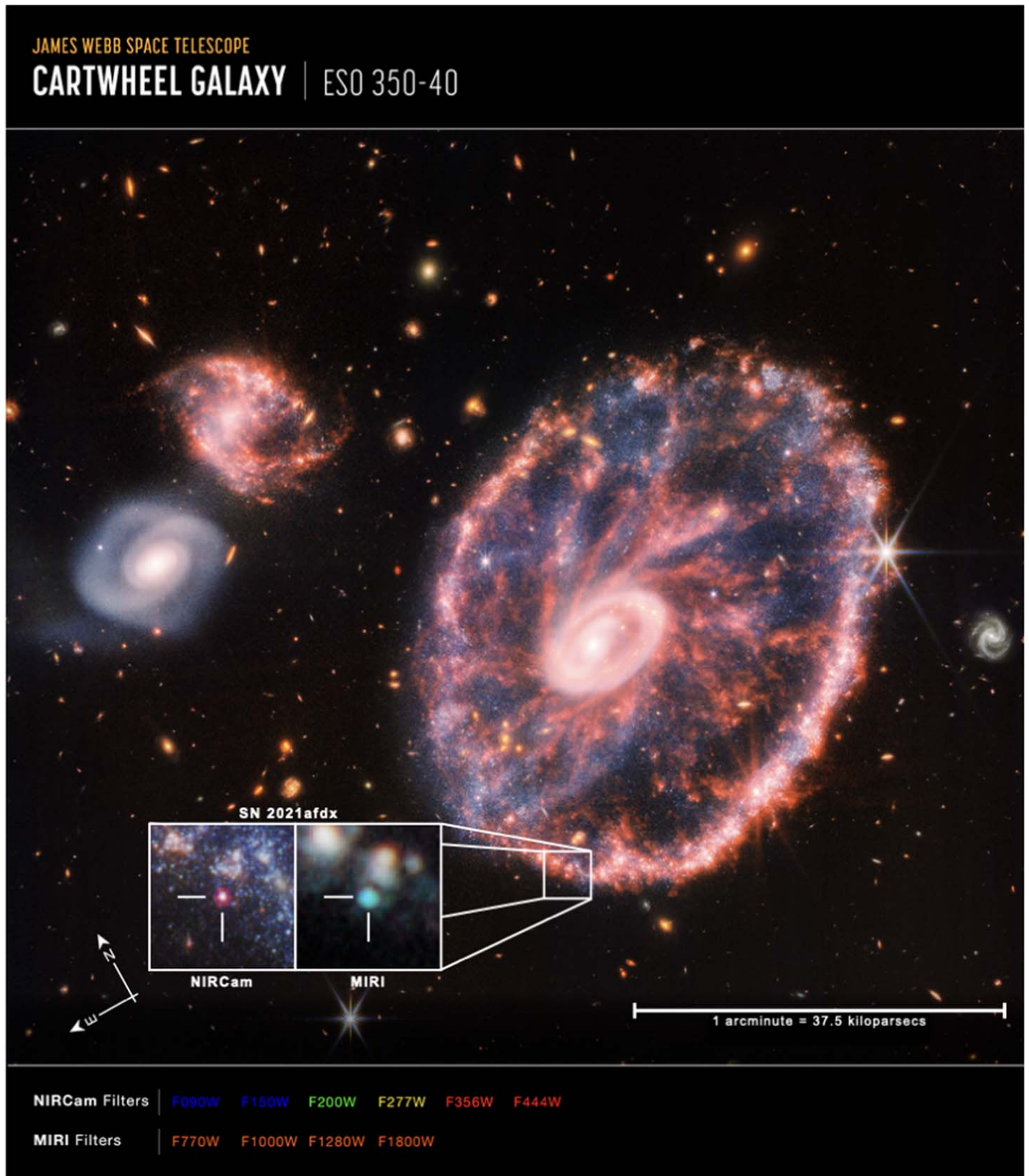


Figure 1. Composite image of the Cartwheel Galaxy taken with JWST’s NIRCam and MIRI instruments, with $7''.6 \times 7''.6$ insets of SN 2021afdx. Credit: NASA, ESA, CSA, STScI, Webb ERO Production Team.

60, and our light curve does not extend to late enough times to observe a potential fall from plateau (~ 100 days), we cannot rule out a fast-declining SN II (i.e., an SN IIL) with some spectroscopic peculiarities. Our analysis does not depend

strongly on the SN type, other than that it is the core collapse of a massive star, so we proceed by using the broader term (SN II) and comparing to both SNe II and IIb whenever possible.

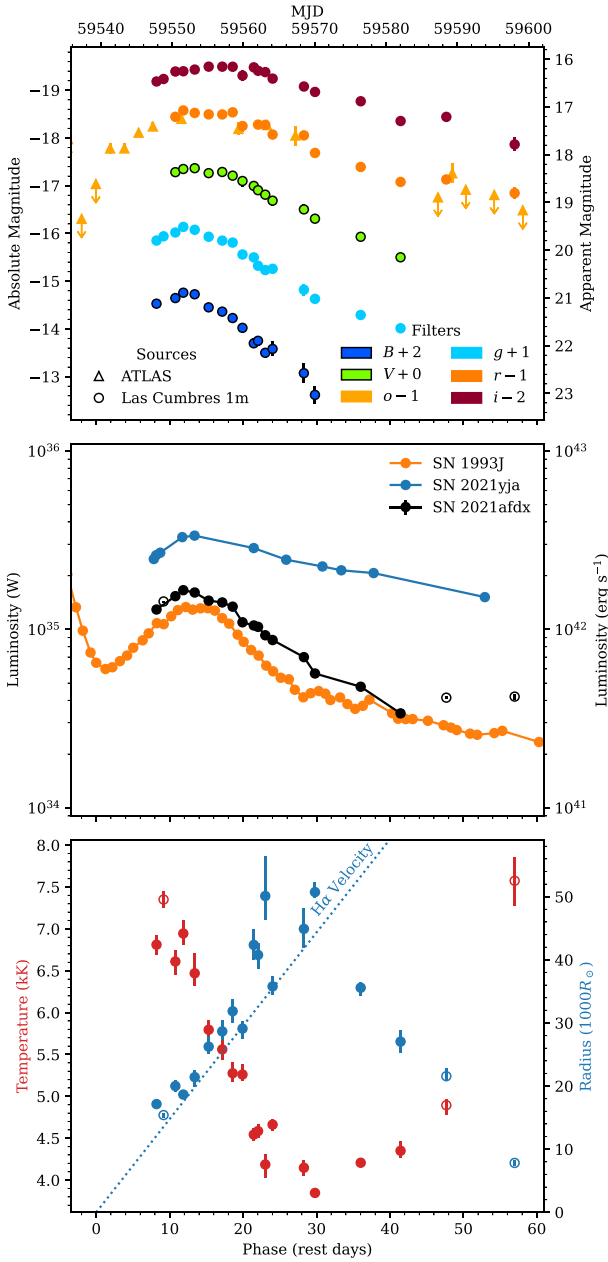


Figure 2. Top: ground-based optical light curve of SN 2021afdx from ATLAS and Las Cumbres Observatory, corrected for Milky Way extinction. Arrows indicate 3σ nondetections. Phases are given with respect to the last pre-discovery nondetection. Center: pseudobolometric (U to I) light curve of SN 2021afdx compared to the pseudobolometric light curves of the Type IIb SN 1993J and the Type II SN 2021yja, approximately aligned to their peak phase. Open markers indicate epochs with detections in only two filters, which may not yield reliable luminosity or temperature measurements. The gradual rise and decline of SN 2021afdx, rather than a rapid rise to a plateau, suggests a Type IIb classification. Bottom: the photospheric temperature (red; left axis) and radius (blue; right axis) of SN 2021afdx derived from the data above. The dotted line shows that the ejecta radius inferred from the measured $H\alpha$ velocity is consistent with the photospheric radius around peak.

(The data used to create this figure are available.)

We measure the photospheric velocity by fitting the sum of two equal-width Gaussians, one positive and one negative, and a linear continuum to the $H\alpha$ feature in each of the first five spectra. The signal-to-noise ratio in the last spectrum is too low to confidently fit the absorption component. We use an MCMC

Table 1
Spectroscopic Observations and Velocities

| MJD | Telescope | Instrument | Phase (day) | $H\alpha$ Velocity (Mm s^{-1}) |
|-----------|-----------|------------|-------------|---|
| 59550.492 | FTS | FLOYDS | 10.8 | 12.59 ± 0.07 |
| 59557.503 | FTS | FLOYDS | 17.6 | 11.70 ± 0.07 |
| 59561.491 | FTS | FLOYDS | 21.5 | 12.1 ± 0.1 |
| 59572.494 | FTS | FLOYDS | 32.2 | 11.9 ± 0.1 |
| 59583.469 | FTS | FLOYDS | 42.8 | 11.1 ± 0.1 |
| 59601.425 | FTS | FLOYDS | 60.3 | ... |

routine with uniform priors on the centers of the Gaussians and the continuum intercept and log-uniform priors on the amplitudes and width of the Gaussians and the continuum slope. We report the means and standard deviations of the velocity posteriors, as calculated from the maximum and minimum of the model minus the continuum, in Table 1. The mean and standard deviation of these five measurements is $v_{ej} \approx 11.9 \pm 0.5 \text{ Mm s}^{-1}$. Figure 2 (bottom) shows that this velocity is consistent with the photospheric radii around peak.

2.2. Space-based Infrared

We downloaded the JWST images of the Cartwheel Galaxy in 10 filters spanning $0.9\text{--}18 \mu\text{m}$ from the Mikulski Archive for Space Telescopes (Proposal 2727; PI: Pontoppidan; doi:10.17909/2n49-hx69) and performed aperture photometry using Photutils (Bradley et al. 2022). For NIRCcam, we used a circular aperture containing 80% of the PSF energy. For MIRI, we used a circular aperture containing 50% of the PSF energy, to avoid contamination from the star-forming region. We then applied aperture corrections from the JWST Calibration Reference Data System (CRDS; Greenfield & Miller 2016). Table 2 lists the results, given in AB magnitudes, and Figure 4 shows cutouts of these 10 images centered on the SN.

The galaxy background in this region is complicated, and in the longer-wavelength filters the flux in the aperture is dominated by instrumental background. Thus, careful background subtraction is required. We chose two 3×3 pixel squares directly above and below the aperture (roughly perpendicular to the nearby star-forming region) and estimated the background level and its uncertainty by taking the median and the median absolute deviation, respectively, of those 18 pixels. Figure 4 shows the source and background apertures in each image, and Table 2 lists the source and background fluxes within the source aperture. We subtracted the background level from each pixel in the aperture and added the background uncertainty in quadrature to the error images provided. The choice of the background level may explain the discrepancy between our measurements and the preliminary photometry of Engesser et al. (2022).

At the time of our analysis, the MIRI aperture corrections had been updated using in-flight data (`jwst_miri_apcorr_0008.fits`), but the NIRCcam aperture corrections had not (`jwst_nircam_apcorr_0004.fits`). In addition, the zero-point calibrations of both instruments suffer from uncertainties relative to preflight expectations. Boyer et al. (2022) report time-variable offsets of 1%–23% in the eight NIRCcam detectors, and the most recent reduced MIRI images suffer from imperfect flat-fielding of up to $\approx 5\%$ uncertainty in flux values. The data at $>18 \mu\text{m}$ has an additional uncertainty on flux zero-point, as their linearity correction coefficients have

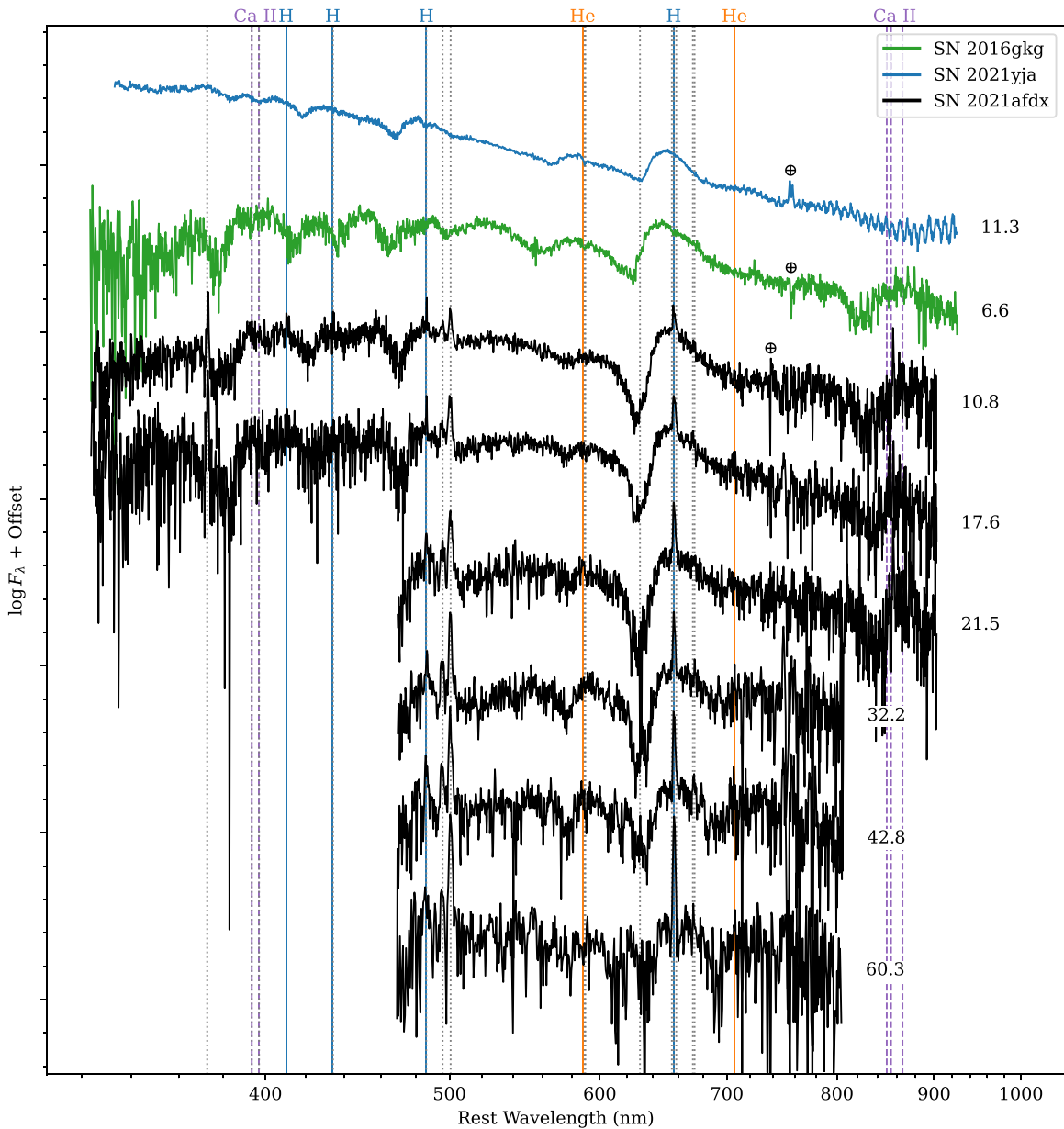


Figure 3. Spectral series of SN 2021afdx compared to spectra of the Type IIb SN 2016gkg and the Type II SN 2021yja, all from FLOYDS. Phases are given to the right of each spectrum in rest-frame days. The latest spectrum is binned by a factor of 2 for clarity. We attribute the narrow emission lines (marked with gray dotted lines) to the underlying star-forming region in the Cartwheel Galaxy. The strongest telluric feature is marked with the \oplus symbol. The remaining features can be explained by P Cygni profiles of hydrogen, helium, and Ca II. The broad, deep, asymmetric hydrogen absorption feature, the high helium-to-hydrogen line ratio, and relatively red continuum suggest a Type IIb classification for SN 2021afdx, although we never observe the hydrogen feature fully disappear.

(The data used to create this figure are available.)

not yet been updated based on in-flight data. We choose to proceed with the official zero-points from CRDS (version 11.16.3), keeping in mind that our results can be reevaluated in the future when more accurate calibrations are established.

3. Dust Modeling

Figure 5 shows the infrared SED of SN 2021afdx at a phase of 197–200 rest-frame days. The most notable feature is a peak in F_λ at 4–7 μm , a second emission component that may indicate dust associated with the SN.

We model the input luminosity as a hot blackbody with temperature T_{phot} and radius R_{phot} plus a uniform sphere of

warm dust with temperature T_{dust} , radius R_{dust} , and mass M_{dust} :

$$L_{\nu,\text{in}} = 4\pi R_{\text{phot}}^2 \pi B_\nu(T_{\text{phot}}) + 4\kappa_\nu M_{\text{dust}} \pi B_\nu(T_{\text{dust}}), \quad (1)$$

where κ_ν is the frequency-dependent opacity of the dust and $B_\nu(T)$ is the Planck (1906) function. We calculate the frequency-dependent opacity κ_ν from the absorption efficiency Q_ν and particle density $\rho_{\text{particle}} = 2.26 \text{ g cm}^{-3}$ of $a = 0.1 \mu\text{m}$ graphite dust given by Laor & Draine (1993):

$$\kappa_\nu = \frac{3Q_\nu}{4a\rho_{\text{particle}}} \quad (2)$$

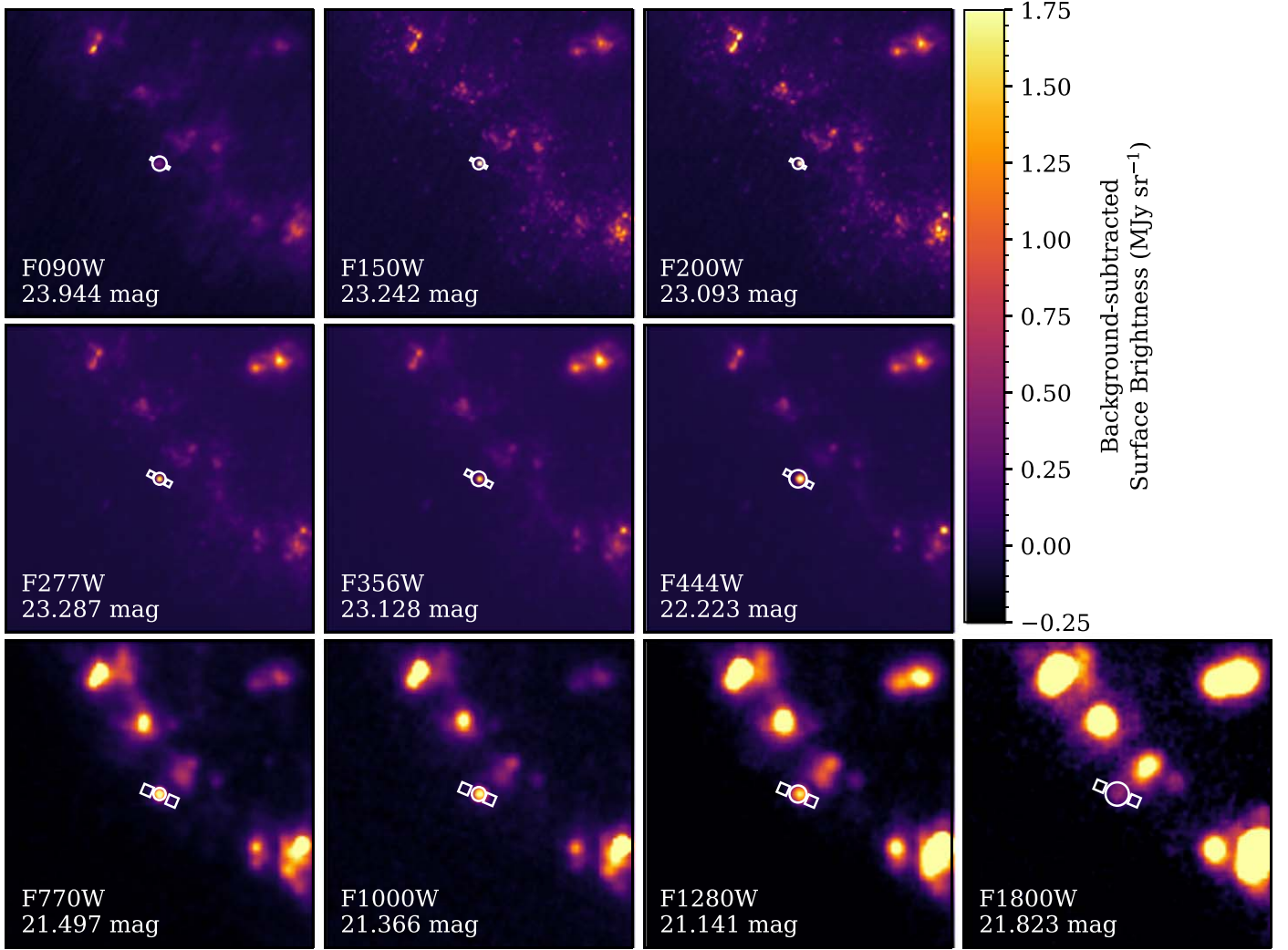


Figure 4. $10'' \times 10''$ cutouts of JWST images of the Cartwheel Galaxy centered on SN 2021afdx in 10 filters. The images are in their native resolution but have been resampled to have north up and east to the left. White circles mark the aperture used for photometry. White squares mark the region used for background subtraction. The filter name and SN brightness (in AB magnitudes) are reported in the lower left corner of each panel.

Table 2
JWST Observations and Photometry

| MJD | Instrument | Filter | Exp. (s) ^a | Magnitude | Flux (μ Jy) | Bkg. Flux (μ Jy) | Phase (d) |
|-----------|------------|--------|-----------------------|--------------------|-------------------|-----------------------|-----------|
| 59742.131 | NIRCam | F090W | 2748.616 | 23.944 ± 0.030 | 0.960 ± 0.018 | 1.553 ± 0.021 | 197 |
| 59742.172 | NIRCam | F150W | 2748.616 | 23.242 ± 0.011 | 1.833 ± 0.012 | 0.927 ± 0.016 | 197 |
| 59742.214 | NIRCam | F200W | 2748.616 | 23.093 ± 0.007 | 2.103 ± 0.011 | 0.713 ± 0.012 | 197 |
| 59742.131 | NIRCam | F277W | 2748.616 | 23.287 ± 0.004 | 1.759 ± 0.006 | 0.499 ± 0.004 | 197 |
| 59742.172 | NIRCam | F356W | 2748.616 | 23.128 ± 0.009 | 2.036 ± 0.015 | 0.696 ± 0.017 | 197 |
| 59742.214 | NIRCam | F444W | 2748.616 | 22.223 ± 0.007 | 4.686 ± 0.022 | 2.244 ± 0.028 | 197 |
| 59745.322 | MIRI | F770W | 4040.464 | 21.497 ± 0.007 | 9.14 ± 0.13 | 22.796 ± 0.047 | 200 |
| 59745.354 | MIRI | F1000W | 4040.464 | 21.366 ± 0.008 | 10.32 ± 0.11 | 71.842 ± 0.037 | 200 |
| 59745.388 | MIRI | F1280W | 4040.464 | 21.141 ± 0.017 | 12.69 ± 0.33 | 184.52 ± 0.17 | 200 |
| 59745.420 | MIRI | F1800W | 4084.864 | 21.823 ± 0.076 | 6.77 ± 0.60 | 1097.60 ± 0.38 | 200 |

Note.

^a Effective exposure time, corrected for dead time and lost time.

Both components are extinguished according to the escape probability from Osterbrock (1989, Appendix 2):

$$p_{\text{esc}} = \frac{3}{4\tau_\nu} \left[1 - \frac{1}{2\tau_\nu^2} + \left(\frac{1}{\tau_\nu} + \frac{1}{2\tau_\nu^2} \right) e^{-2\tau_\nu} \right], \quad (3)$$

where the frequency-dependent optical depth to the center of the dust sphere with bulk density ρ_{bulk} is

$$\tau_\nu = \kappa_\nu \rho_{\text{bulk}} R_{\text{dust}} = \frac{3\kappa_\nu M_{\text{dust}}}{4\pi R_{\text{dust}}^2}. \quad (4)$$

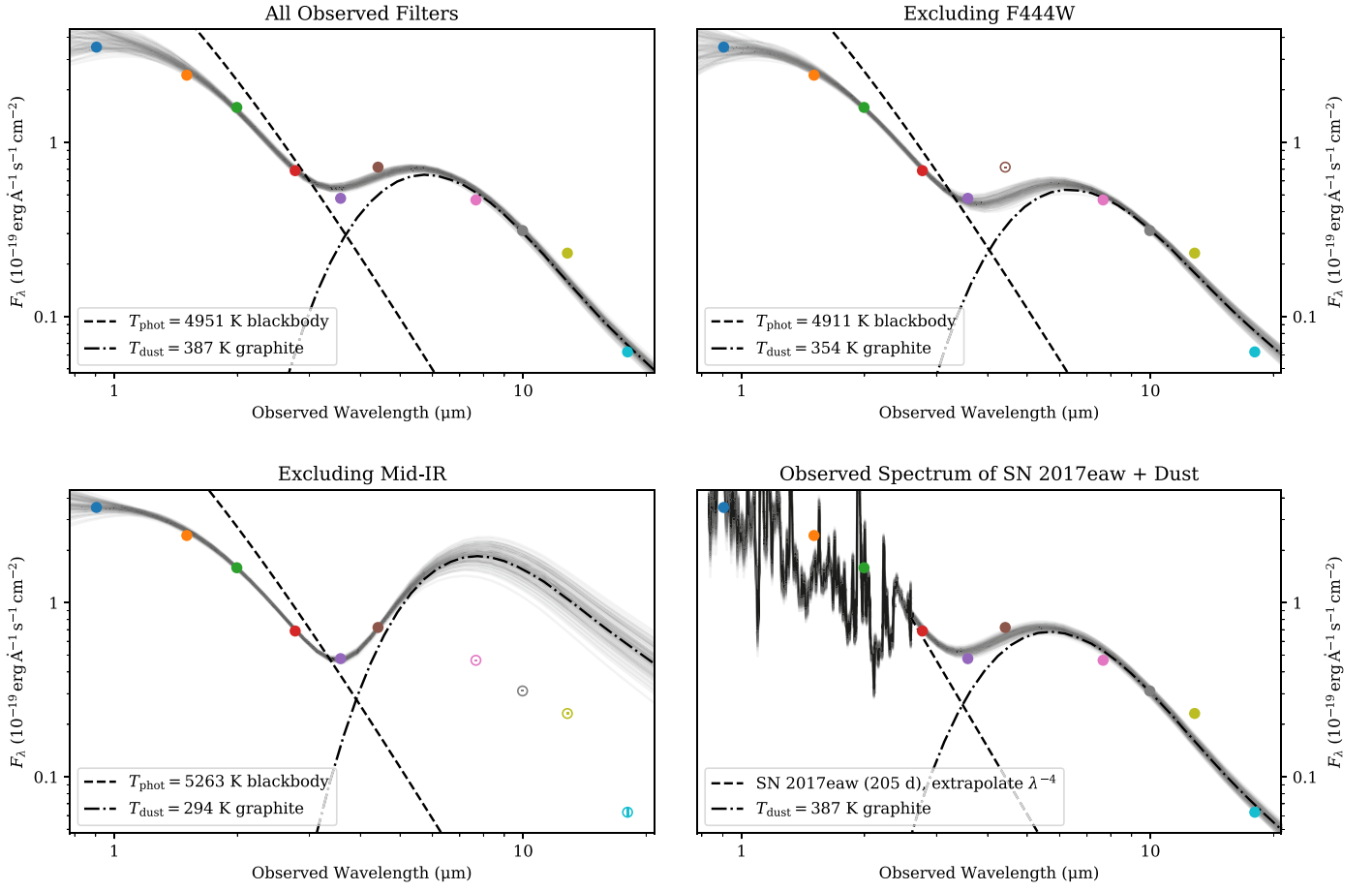


Figure 5. Top left: the IR SED of SN 2021afdx at a phase of 197–200 rest-frame days (circles), compared to models of dust emission (solid lines). The dashed line shows the hot blackbody component without extinction and the dotted–dashed line shows the warm graphite dust component. The dotted line shows a blackbody with the same temperature and radius as the dust. The blackbody plus dust model describes our observations well. Top right: same as left, but excluding F444W from the fit (open circle). This filter may be contaminated by carbon monoxide emission. Excluding it gives a slightly better fit to the remaining data points, so we adopt this as our preferred model. Bottom left: same as above, but excluding all filters redward of F444W (open circles), i.e., all the mid-IR observations. This wavelength coverage is analogous to previous SN observations with the Spitzer Warm Mission. The dust SED is very poorly constrained and is not consistent with our mid-IR observations, leading to incorrect inferences about the dust properties. Bottom right: same as others, but using the observed spectrum of SN 2017eaw (Rho et al. 2018), extrapolated as λ^{-4} (dashed line), to model the near-IR filters. The resulting dust parameters are nearly identical to the blackbody fit (top left) but with a slightly higher intrinsic scatter.

Therefore, the full model SED is

$$L_\nu = \left[4\pi R_{\text{phot}}^2 \pi B_\nu(T_{\text{phot}}) \frac{3}{4\tau_\nu} + 4\pi R_{\text{dust}}^2 \pi B_\nu(T_{\text{dust}}) \right] \times \left[1 - \frac{1}{2\tau_\nu^2} + \left(\frac{1}{\tau_\nu} + \frac{1}{2\tau_\nu^2} \right) e^{-2\tau_\nu} \right]. \quad (5)$$

In the optically thin limit ($\tau_\nu \ll 1$), Equation (5) reduces to Equation (1), in which case R_{dust} will not be well constrained. In the optically thick limit ($\tau_\nu \gg 1$), the second term in square brackets in Equation (5) approaches unity, in which case M_{dust} cannot be constrained independently of R_{phot} .

We fit this model to the observed SED using an MCMC routine implemented in the Light Curve Fitting package (Hosseinzadeh & Gomez 2022). We also include an intrinsic scatter term, σ , that accounts for uncertainties in the model (e.g., line emission) by inflating the error bars on each data point by a factor of $\sqrt{1 + \sigma^2}$. We run 20 walkers for 2000 steps to reach convergence and then another 1000 steps to sample the posterior. Table 3 lists the model parameters, their

priors, and their best-fit values (median and 1σ equal-tailed credible interval). The best-fit model, as well as a breakdown of the two components, is shown in Figure 5 (top left).

SNe II (including SNe IIB) are known to produce carbon monoxide (CO) during the nebular phase (e.g., Catchpole et al. 1988; Spyromilio et al. 1988; Spyromilio & Leibundgut 1996; Ergon et al. 2015), whose fundamental rovibrational transition emits around $4.6 \mu\text{m}$. If CO is present in SN 2021afdx, this will produce an excess in our F444W observation with respect to the dust model. Therefore we repeat the above modeling procedure excluding this filter. Figure 5 (top right) and Table 3 show the results. This indeed achieves a better fit ($\sigma = 3.9$ versus 6.0) with a slightly lower dust temperature, under-shooting F444W. We therefore adopt these results as our preferred set of parameters and claim a tentative detection of CO.

As a demonstration of the power of JWST in the mid-IR, we also repeat the fit excluding the four mid-IR filters (F770W, F1000W, F1280W, and F1800W). This fit simulates a data set from the Spitzer Warm Mission, the best IR data available over the past decade. Figure 5 (bottom left) and Table 3 show that the dust SED is very poorly constrained without the mid-IR

Table 3
Dust Model Parameters

| Parameter | Prior | 1σ Equal-tailed Credible Interval | | | | Unit |
|--------------------------|--------------------------------------|--|---------------------------|---------------------------|---------------------------|---------------------|
| | | All Filters | No F444W | No Mid-IR | SN 2017eaw | |
| Photospheric temperature | Uniform(0.1, 100) | 5^{+2}_{-1} | 5 ± 1 | $5.3^{+0.7}_{-0.5}$ | ... | kK |
| Photospheric radius | Log-uniform(0.01, 1000) | $4.6^{+0.8}_{-0.7}$ | $4.9^{+1.0}_{-0.5}$ | 4.8 ± 0.3 | ... | $1000 R_{\odot}$ |
| Dust temperature | Uniform(0.1, 100) | $0.387^{+0.006}_{-0.005}$ | $0.354^{+0.006}_{-0.008}$ | $0.294^{+0.007}_{-0.006}$ | $0.387^{+0.005}_{-0.006}$ | kK |
| Dust radius | Log-uniform(0.01, 5000) ^a | 1700^{+800}_{-400} | 1800^{+1200}_{-300} | 5700^{+1100}_{-800} | 5000^{+2000}_{-1000} | $1000 R_{\odot}$ |
| Dust mass | Log-uniform(1, 1000) | 2.5 ± 0.2 | $3.8^{+0.5}_{-0.3}$ | 40 ± 10 | 2.5 ± 0.2 | $10^{-3} M_{\odot}$ |
| Intrinsic scatter | Half-Gaussian(max = 8) ^a | 6.0 ± 0.5 | $3.9^{+0.6}_{-0.4}$ | $2.1^{+0.6}_{-0.4}$ | 7.4 ± 0.5 | ... |

Note.

^a For the fit excluding the mid-IR filters, we extend the maximum on R_{dust} to $10^7 R_{\odot}$ and reduce the prior on σ to 6. For the fit with SN 2017eaw, we extend the maximum on R_{dust} to $10^7 R_{\odot}$ and increase the prior on σ to 10.

data points, and it leads to incorrect inferences about the dust properties.

At ≈ 200 days, the near-IR SEDs of SNe may not be well approximated by a blackbody, due to strong nebular emission lines. Therefore, as a final check, we repeat the fit using a model in which the hot blackbody is replaced by the observed spectrum of the Type II SN 2017eaw at 205 days after explosion from Rho et al. (2018), multiplied by a constant. We extrapolate from 2.52 to $19.5 \mu\text{m}$ (although it is negligible at $\gtrsim 5 \mu\text{m}$) using a λ^{-4} power law (Rayleigh 1900) matched to the red tail of the observed spectrum. The results, shown in Figure 5 (bottom right) and Table 3, give nearly identical dust parameters to the original fit with a blackbody, but with slightly higher intrinsic scatter.

Thanks to our simultaneous near-IR observations, which do not appear to suffer from significant extinction, we can conclude that the dust producing the mid-IR peak is optically thin. This implies a large radius for the dust sphere, on which our fitting procedure can only provide a lower limit, or deviations from our uniform spherical model (e.g., larger grains, clumps, or a nonspherical distribution). We discuss this further in Section 4. However, because the dust sphere is optically thin, the fit provides a true measurement of the dust mass: $M_{\text{dust}} = (3.8^{+0.5}_{-0.3}) \times 10^{-3} M_{\odot}$. This is consistent with most of the distribution of SN II dust masses from Szalai et al. (2019, see Figure 6) and Niculescu-Duvaz et al. 2022, although almost all of their observations are at later phases than ours. Notably, our limit is higher than the dust masses in any of the four SNe IIB observed by Szalai et al. (2019). The significance of this result will only become clear with larger sample sizes of the rarer subclasses of core-collapse SNe.

4. Dust Formation Scenarios

Given these measurements, we investigate whether the dust that we observe is newly formed in the SN ejecta or whether it existed in the circumstellar environment prior to explosion. Optical observations at this phase could show the effect of dust extinction on the broadband light curve or the spectroscopic line profiles, but at this late phase, SN 2021afdx is beyond the reach of most ground-based telescopes. Therefore we must rely only on the parameters from our IR SED modeling. In the newly formed dust scenario, we would expect the dust radius to be consistent with the ejecta radius and the dust temperature to be near the condensation temperature.

Using the mean $H\alpha$ velocities from Section 2.1 and assuming homologous expansion, we estimate the ejecta

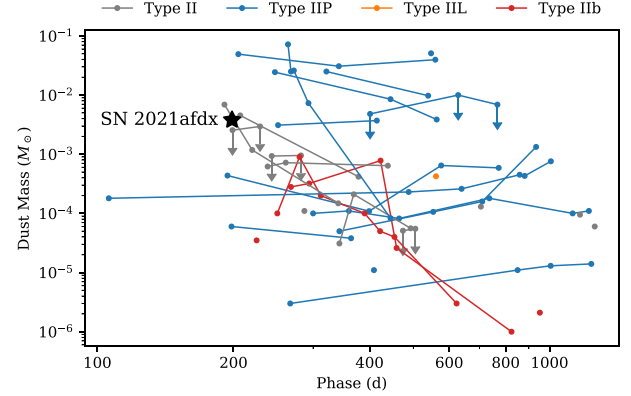


Figure 6. Dust masses in SNe II observed by Spitzer (circles) from Szalai et al. (2019). Lines connect multiple measurements for individual SNe, and downward-pointing arrows indicate upper limits on dust masses when reference images for subtraction were not available. The dust mass of SN 2021afdx measured here (black star) is consistent with most of their distribution. Notably, our measurement is higher than the dust masses in any of the previously observed SNe IIB, although the sample size is small.

position to be $R_{\text{ej}}(t) = v_{\text{ej}}t = (2.9 \pm 0.1) \times 10^5 R_{\odot}$, which is smaller than the 3σ lower limit on the dust radius from Section 3. Therefore the dust likely extends beyond, or lies entirely outside of, the SN ejecta. Theory predicts the condensation temperature for carbonaceous dust to be $\gtrsim 1600$ K (Gall et al. 2011b), about 4.5 times our measured dust temperature. However, astrophysical evidence from both massive stars (e.g., Beasor & Davies 2016; Lau et al. 2021) and SNe (e.g., Tinyanont et al. 2016; Szalai et al. 2019) points to condensation temperatures below 1000 K, so we do not consider this a point against the newly formed dust scenario.

The alternative is that we are seeing an IR echo (e.g., Bode & Evans 1980; Dwek 1983; Graham & Meikle 1986; Meikle et al. 2006) off of preexisting dust in the circumstellar environment. We can check the consistency of this scenario with an equilibrium calculation: each dust grain must emit as much energy as it absorbs. The luminosity emitted by an individual dust grain with radius $a = 0.1 \mu\text{m}$ and temperature $T_{\text{dust}} = 354$ K is

$$L_{\text{em}} = 4\pi a^2 \pi \int B_{\nu}(T_{\text{dust}}) Q_{\nu} d\nu. \quad (6)$$

The luminosity absorbed by this dust grain from a source with photospheric radius $R_{\text{peak}} = 18,700 R_{\odot}$ and temperature

$T_{\text{peak}} = 6900$ K at a distance R_{dust} is

$$L_{\text{abs}} = \pi a^2 \pi \int B_{\nu}(T_{\text{peak}}) Q_{\nu} d\nu \frac{R_{\text{peak}}^2}{R_{\text{dust}}^2}. \quad (7)$$

Setting Equation (6) equal to Equation (7), we can solve for the radius of the dust shell.¹² We find that the dust must lie at $R_{\text{dust}} = 3.5 \times 10^7 R_{\odot} = 935$ light-days from the center of the explosion. This is fully consistent with the dust radius from Section 3. Therefore we conclude that SN 2021afdx likely had dust in its circumstellar environment prior to explosion.

Although we cannot yet have observed the light reradiated from the entire sphere of dust due to light-travel time, we may be seeing emission only from the dust near the line of sight. If our interpretation is correct, further JWST observations of SN 2021afdx would show dust at this temperature for ≈ 2000 days before it begins to fade. However, this could also be a similar case to the Type IIb SN 2011dh, which showed an IR echo from preexisting dust for the first ≈ 100 days but required newly formed dust or additional heating mechanisms to explain the IR light curve at $\gtrsim 250$ days (Helou et al. 2013).

5. Summary and Conclusions

We have presented near- and mid-IR observations of SN 2021afdx taken with JWST. The unprecedented combination of wavelength coverage (0.9–18 μm) and sensitivity allows us to distinguish two distinct components in the nebular IR SED, which we attribute to hot ejecta and warm dust. By fitting models of dust emission to the SED, we measure the mass of dust to be $M_{\text{dust}} = (3.8_{-0.3}^{+0.5}) \times 10^{-3} M_{\odot}$, which is fairly typical among core-collapse SNe at this phase and higher than all previously observed SNe IIb dust masses. We find that the radius of the dust sphere is significantly larger than the ejecta position at this phase, suggesting that we are seeing an IR echo off of preexisting dust in the progenitor environment. This means that SN 2021afdx has not (yet) produced dust in the amount needed to explain observations of galaxies in the early universe.

This Letter demonstrates the power of JWST to constrain models of SN dust formation, a capability that has been missing since the Spitzer Cold Mission. Furthermore, SN 2021afdx is almost twice as distant as the farthest SN II observed by Spitzer in the nebular phase (Szalai et al. 2019), meaning that many more nebular SNe, including those of rarer subtypes (e.g., SNe IIb), will be observable by JWST in the coming years. This increased sample size will quickly begin to probe the extent to which interstellar dust formation in the early universe can be explained by SNe.

We thank Matteo Correnti for his JWST postpipeline data analysis notebook,¹³ which provided a starting point for our analysis, Samaporn Tinyanont for maintaining publicly available, machine-readable graphite opacity tables,¹⁴ and Jeonghee Rho for providing her spectrum of SN 2017eaw. We also thank Emma Beasor and Ryan Lau for helpful discussions about dust

formation. Lastly, we thank the anonymous referee, whose careful consideration greatly improved this work.

This work is based on observations made with the NASA/ESA/CSA James Webb Space Telescope. The data were obtained from the Mikulski Archive for Space Telescopes at the Space Telescope Science Institute, which is operated by the Association of Universities for Research in Astronomy, Inc., under NASA contract NAS 5-03127 for JWST. These observations are associated with program #2727. The Early Release Observations and associated materials were developed, executed, and compiled by the ERO production team: Hannah Braun, Claire Blome, Matthew Brown, Margaret Carruthers, Dan Coe, Joseph DePasquale, Nestor Espinoza, Macarena Garcia Marin, Karl Gordon, Alaina Henry, Leah Hustak, Andi James, Ann Jenkins, Anton Koekemoer, Stephanie LaMassa, David Law, Alexandra Lockwood, Amaya Moro-Martin, Susan Mullally, Alyssa Pagan, Dani Player, Klaus Pontoppidan, Charles Proffitt, Christine Pulliam, Leah Ramsay, Swara Ravindranath, Neill Reid, Massimo Robberto, Elena Sabbi, and Leonardo Ubeda. The EROs were also made possible by the foundational efforts and support from the JWST instruments, STScI planning and scheduling, and Data Management teams. The authors acknowledge the ERO production team for developing their observing program with a zero-exclusive-access period. This work makes use of data from the Las Cumbres Observatory telescope network.

Time domain research by G.H, D.J.S, and the University of Arizona team is supported by NSF grants AST-1821987, 1813466, 1908972, and 2108032, and by the Heising-Simons Foundation under grant #2020-1864. J.E.A. is supported by the international Gemini Observatory, a program of NSF's NOIRLab, which is managed by the Association of Universities for Research in Astronomy (AURA) under a cooperative agreement with the National Science Foundation, on behalf of the Gemini partnership of Argentina, Brazil, Canada, Chile, the Republic of Korea, and the United States of America. Research by S.V. is supported by NSF grant AST-2008108. T.S. is supported by the NKFIH/OTKA FK-134432 grant of the National Research, Development and Innovation (NRDI) Office of Hungary, the János Bolyai Research Scholarship of the Hungarian Academy of Sciences, and the New National Excellence Program (ÚNKP-21-5) of the Ministry for Innovation and Technology of Hungary from the source of NRDI Fund. The Las Cumbres Observatory group is supported by NSF grants AST-1911225 and 1911151.

Facilities: ADS, JWST (MIRI, NIRCam), LCOGT (FLOYDS, Sinistro), OSC, NED, TNS.

Software: Astropy (Astropy Collaboration et al. 2022), emcee (Foreman-Mackey et al. 2013), FLOYDS pipeline (Valenti et al. 2014), `lcogtsnpipe` (Valenti et al. 2016), Light Curve Fitting (Hosseinzadeh & Gomez 2022), JWST CRDS (Greenfield & Miller 2016), Photutils (Bradley et al. 2022), PyZOGY (Guevel & Hosseinzadeh 2017).

ORCID iDs

Griffin Hosseinzadeh  <https://orcid.org/0000-0002-0832-2974>

David J. Sand  <https://orcid.org/0000-0003-4102-380X>

Jacob E. Jencson  <https://orcid.org/0000-0001-5754-4007>











Jennifer E. Andrews  <https://orcid.org/0000-0003-0123-0062>

Irene Shivaie  <https://orcid.org/0000-0003-4702-7561>

¹² Note that the result is not fully independent of a because the efficiency curve Q_{ν} depends on the dust grain size.

¹³ <https://jwst-docs.stsci.edu/jwst-post-pipeline-data-analysis/data-analysis-example-jupyter-notebooks>

¹⁴ https://github.com/stinyanont/sed_et_al

K. Azalee Bostroem  <https://orcid.org/0000-0002-4924-444X>
 Stefano Valenti  <https://orcid.org/0000-0001-8818-0795>
 Tamás Szalai  <https://orcid.org/0000-0003-4610-1117>
 Jamison Burke  <https://orcid.org/0000-0003-0035-6659>
 D. Andrew Howell  <https://orcid.org/0000-0003-4253-656X>
 Curtis McCully  <https://orcid.org/0000-0001-5807-7893>
 Megan Newsome  <https://orcid.org/0000-0001-9570-0584>
 Estefania Padilla Gonzalez  <https://orcid.org/0000-0003-0209-9246>
 Craig Pellegrino  <https://orcid.org/0000-0002-7472-1279>
 Giacomo Terreran  <https://orcid.org/0000-0003-0794-5982>

References

- Amram, P., Mendes de Oliveira, C., Boulesteix, J., & Balkowski, C. 1998, *A&A*, **330**, 881
- Andrews, J. E., Sugerma, B. E. K., Clayton, G. C., et al. 2011, *ApJ*, **731**, 47
- Arendt, R. G., Dwek, E., Kober, G., Rho, J., & Hwang, U. 2014, *ApJ*, **786**, 55
- Astropy Collaboration, Price-Whelan, A. M., Lim, P. L., et al. 2022, *ApJ*, **935**, 167
- Bakx, T. J. L. C., Tamura, Y., Hashimoto, T., et al. 2020, *MNRAS*, **493**, 4294
- Barbon, R., Benetti, S., Cappellaro, E., et al. 1995, *A&AS*, **110**, 513
- Barlow, M. J., Krause, O., Swinyard, B. M., et al. 2010, *A&A*, **518**, L138
- Beasor, R., & Davies, B. 2016, *MNRAS*, **463**, 1269
- Benson, P. J., Herbst, W., Salzer, J. J., et al. 1994, *AJ*, **107**, 1453
- Bertoldi, F., Cox, P., Neri, R., et al. 2003, *A&A*, **409**, L47
- Bode, M. F., & Evans, A. 1980, *MNRAS*, **193**, 21P
- Boyer, M. L., Anderson, J., Gennaro, M., et al. 2022, *RNAAS*, **6**, 191
- Bradley, L., Sipőcz, B., Robitaille, T., et al. 2022, *Astropy/Photutils*: v1.5.0, Zenodo, doi:10.5281/zenodo.6825092
- Brown, T. M., Baliber, N., Bianco, F. B., et al. 2013, *PASP*, **125**, 1031
- Buzzoni, B., Delabre, B., Dekker, H., et al. 1984, *Msngr*, **38**, 9
- Catchpole, R. M., Whitelock, P. A., Feast, M. W., et al. 1988, *MNRAS*, **231**, 75P
- De Looze, I., Barlow, M. J., Swinyard, B. M., et al. 2017, *MNRAS*, **465**, 3309
- Dwek, E. 1983, *ApJ*, **274**, 175
- Dwek, E., Galliano, F., & Jones, A. P. 2007, *ApJ*, **662**, 927
- Dwek, E., Sarangi, A., & Arendt, R. G. 2019, *ApJL*, **871**, L33
- Engesser, M., Smith, K., Chen, T., et al. 2022, *TNSAN*, **155**, 1
- Ergon, M., Jerkstrand, A., Sollerman, J., et al. 2015, *A&A*, **580**, A142
- Fitzpatrick, E. L. 1999, *PASP*, **111**, 63
- Foreman-Mackey, D., Hogg, D. W., Lang, D., & Goodman, J. 2013, *PASP*, **125**, 306
- Fox, O. D., Chevalier, R. A., Dwek, E., et al. 2010, *ApJ*, **725**, 1768
- Fox, O. D., Chevalier, R. A., Skrutskie, M. F., et al. 2011, *ApJ*, **741**, 7
- Gall, C., Andersen, A. C., & Hjorth, J. 2011a, *A&A*, **528**, A13
- Gall, C., Hjorth, J., & Andersen, A. C. 2011b, *A&ARv*, **19**, 43
- Gal-Yam, A. 2016, in *Handbook of Supernovae*, ed. A. W. Alsabti & P. Murdin (Cham: Springer)
- Gomez, H. L., Krause, O., Barlow, M. J., et al. 2012, *ApJ*, **760**, 96
- Graham, J. R., & Meikle, W. P. S. 1986, *MNRAS*, **221**, 789
- Greenfield, P., & Miller, T. 2016, *A&C*, **16**, 41
- Guevel, D., Hosseinzadeh, G., Bostroem, K. A., & Burke, C. J. 2021, *PyZOGY* v0.0.2, Zenodo, doi:10.5281/zenodo.4570234
- Hashimoto, T., Inoue, A. K., Mawatari, K., et al. 2019, *PASJ*, **71**, 71
- Helou, G., Kasliwal, M. M., Ofek, E. O., et al. 2013, *ApJL*, **778**, L19
- Henden, A. A., Welch, D. L., Terrell, D., & Levine, S. E. 2009, *BAAS*, **41**, 669
- Hosseinzadeh, G., & Gomez, S. 2022, *Light Curve Fitting v0.7.0*, Zenodo, doi:10.5281/zenodo.4312178
- Hosseinzadeh, G., Kilpatrick, C. D., Dong, Y., et al. 2022, *ApJ*, **935**, 31
- Indebetouw, R., Matsuura, M., Dwek, E., et al. 2014, *ApJ*, **782**, L2
- Kotak, R., Meikle, P., Pozzo, M., et al. 2006, *ApJL*, **651**, L117
- Kotak, R., Meikle, P., van Dyk, S. D., Hoflich, P. A., & Mattila, S. 2005, *ApJL*, **628**, L123
- Kotak, R., Meikle, W. P. S., Farrah, D., et al. 2009, *ApJ*, **704**, 306
- Laor, A., & Draine, B. T. 1993, *ApJ*, **402**, 441
- Lau, R. M., Hankins, M. J., Kasliwal, M. M., et al. 2021, *ApJ*, **909**, 113
- Lau, R. M., Herter, T. L., Morris, M. R., Li, Z., & Adams, J. D. 2015, *Sci*, **348**, 413
- Lewis, J. R., Walton, N. A., Meikle, W. P. S., et al. 1994, *MNRAS*, **266**, L27
- Matsuura, M., Dwek, E., Meixner, M., et al. 2011, *Sci*, **333**, 1258
- Meikle, W. P. S., Kotak, R., Farrah, D., et al. 2011, *ApJ*, **732**, 109
- Meikle, W. P. S., Mattila, S., Gerardy, C. L., et al. 2006, *ApJ*, **649**, 332
- Meikle, W. P. S., Mattila, S., Pastorello, A., et al. 2007, *ApJ*, **665**, 608
- Metlova, N. V., Tsvetkov, D. Y., Shugarov, S. Y., Esipov, V. F., & Pavlyuk, N. N. 1995, *AstL*, **21**, 598
- Niculescu-Duvaz, M., Barlow, M. J., Bevan, A., et al. 2022, *MNRAS*, **515**, 4302
- Okyudo, M., Kato, T., Ishida, T., Tokimasa, N., & Yamaoka, H. 1993, *PASJ*, **45**, L63
- Osterbrock, D. E., & Miller, J. S. 1989, *Astrophysics of Gaseous Nebulae and Active Galactic Nuclei* (Sausalito, CA: Univ. Science Books)
- Planck, M. 1906, *Vorlesungen Über Die Theorie Der Wärmestrahlung* (Leipzig: J. A. Barth)
- Planck Collaboration, Aghanim, N., Akrami, Y., et al. 2020, *A&A*, **641**, A6
- Pontoppidan, K. M., Barrientes, J., Blome, C., et al. 2022, *ApJL*, **936**, L14
- Priestley, F. D., Bevan, A., Barlow, M. J., & De Looze, I. 2020, *MNRAS*, **497**, 2227
- Ragosta, F., Carini, R., Tartaglia, L., et al. 2021b, *TNSAN*, **298**, 1
- Ragosta, F., Carini, R., Tartaglia, L., Benetti, S., & Yaron, O. 2021a, *TNSCR*, **4035**, 1
- Rayleigh, L. 1900, *PMag*, **49**, 539
- Rho, J., Geballe, T. R., Banerjee, D. P. K., et al. 2018, *ApJL*, **864**, L20
- Richmond, M. W., Treffers, R. R., Filippenko, A. V., et al. 1994, *AJ*, **107**, 1022
- Richmond, M. W., Treffers, R. R., Filippenko, A. V., & Paik, Y. 1996, *AJ*, **112**, 732
- Rieke, G. H., Wright, G. S., Boker, T., et al. 2015, *PASP*, **127**, 584
- Rieke, M. J., Kelly, D. M., & Horner, S. D. 2005, *Proc. SPIE*, **5904**, 590401
- Schlafly, E. F., & Finkbeiner, D. P. 2011, *ApJ*, **737**, 103
- Smartt, S. J. 2009, *ARA&A*, **47**, 63
- Smartt, S. J., Valenti, S., Fraser, M., et al. 2015, *A&A*, **579**, A40
- Spyromilio, J., & Leibundgut, B. 1996, *MNRAS*, **283**, L89
- Spyromilio, J., Meikle, W. P. S., Learner, R. C. M., & Allen, D. A. 1988, *Natur*, **334**, 327
- Szalai, T., & Vinkó, J. 2013, *A&A*, **549**, A79
- Szalai, T., Vinkó, J., Balog, Z., et al. 2011, *A&A*, **527**, A61
- Szalai, T., Zsíros, S., Fox, O. D., Pejcha, O., & Muller, T. 2019, *ApJS*, **241**, 38
- Tartaglia, L., Fraser, M., Sand, D. J., et al. 2017, *ApJL*, **836**, L12
- Temim, T., Dwek, E., Arendt, R. G., et al. 2017, *ApJ*, **836**, 129
- Tinyanont, S., Kasliwal, M. M., Fox, O. D., et al. 2016, *ApJ*, **833**, 231
- Tonry, J. L., Denneau, L., Weiland, H., et al. 2021, *TNSSTR*, **4000**, 1
- Tonry, J. L., Denneau, L., Heinze, A. N., et al. 2018, *PASP*, **130**, 064505
- Valenti, S., Howell, D. A., Stritzinger, M. D., et al. 2016, *MNRAS*, **459**, 3939
- Valenti, S., Sand, D., Pastorello, A., et al. 2014, *MNRAS*, **438**, L101
- van Driel, W., Yoshida, S., Nakada, Y., et al. 1993, *PASJ*, **45**, L59
- Van Dyk, S. D. 2016, in *Handbook of Supernovae*, ed. A. W. Alsabti & P. Murdin (Cham: Springer)
- Wesson, R., & Bevan, A. 2021, *ApJ*, **923**, 148
- Yaron, O., & Gal-Yam, A. 2012, *PASP*, **124**, 668